# 1

# Two-dimensional Dielectric Photonic Crystals

In Chapter 1, the fundamental concepts for the exploitation of light propagation in photonic crystals are reviewed, based on the exploitation of band structures and equi-frequency surfaces. Special attention is devoted to hole and pillar dielectric lattice nanofabrication techniques, aiming to operate for wavelengths at the micron scale.



## 1.1. Context

As mentioned in the introduction, "dispersion engineering" covers quite a large field of research related to waves, whether acoustic, electromagnetic or optical. Most of these works find their origin in the seminal papers of three extremely brilliant scientists, respectively, V. Veselago, who imagined the possible existence (and potential consequences) of materials with positive and/or negative structural parameters (permittivity and permeability), Sir J. Pendry, who gave proposals to bring these materials to reality, and E. Yablonovitch with his pioneering works on periodic structures (generally labeled photonic crystals) able to tailor photon propagation properties as semiconductors act for electrons. All these concepts can be summarized under the acronym "artificial materials" meaning the creation of materials with properties that cannot be found in nature.

Starting from metals and dielectrics, the common feature of all these approaches is to machine materials at scales lower than the targeted wavelength of operation in order to obtain unusual effective permittivity and permeability (or refractive index/surface impedance) values, for example lower than unity or negative. Depending on the structuring scale, this gives rise to the development of two main classes of materials, respectively metamaterials and electromagnetic or photonic crystals. For the first class of materials, the structuring scale is much lower than the wavelength (λ), typically lower than λ/10. For the second, the structuring scale is closer than λ/2 or λ/4. Depending on the wavelength range targeted, both metal and dielectrics have been widely used as constituents, especially in microwaves up to the terahertz. As the infrared or visible ranges are reached, metals are used less and less, due to high loss levels, and fabrication technologies have limitations in fulfilling the requisite of λ/10… All these reasons explain why the field of "dielectric photonic crystals" appears more developed and mature in optics compared to "metamaterials".

For these wavelengths, around a few micrometers or several hundred nanometers, it soon appeared that three-dimensional (3D) structuring was a considerable challenge needing the development of specific technological equipment and processes. In addition, the main field of applications stems from integrated photonics (or nanophotonics) for which a 2D½ patterning of matter seems to be sufficient. In fact, light will first be confined to a plane, using semiconductor hetero-structures or thin membrane approaches, and its propagation properties fixed by a two-dimensional (2D) patterning of the supporting medium. Using an effective refraction index to define a unique planar dominant propagating mode, "2D dispersion engineering" can then be used to control light propagation in the plane.

This chapter will be divided into three main parts: firstly, the basic concepts of band structures and equi-frequency surfaces will be detailed in the case of 2D dielectric photonic crystals. Secondly, fundamental dispersion effects when such a crystal of finite dimension is interfaced with air (or any other dielectrics) will be reviewed. Thirdly, fabrication aspects to bring all these concepts to reality with solutions issued from semiconductor technology will be outlined.

## 1.2. Concepts: photonic band structures and equi-frequency curves

Photonic crystals (PhCs) are optical semiconductors that dramatically modify electromagnetic wave propagation. Similar to their electronic counterpart, the periodic modulation of the potential function, i.e. the optical index, generates a photonic band structure composed of "allowed" and "forbidden" bands of frequencies for photons. Opening photonic band gaps was the initial motivation of E. Yablonovitch and S. John, the co-inventors of the concept of PhCs. In this regime, lattice defects such as microcavities introduced into PhCs in fact generate localized modes that enable smart engineering at the wavelength scale. This approach has been intensively studied for telecommunications applications, such as for laser or waveguide realizations. In 1998, H. Kosaka proposed an alternative approach to control the photon flow based on the use of the "allowed" photonic bands. Here, the richness of the dispersion curves allows beam-shaping operations that do not require breaking of the lattice symmetry with additional defects. This idea led to the demonstration of new optical effects such as the superprism and self-collimation effects. Beyond this new avenue for the realization of integrated optical components, the ability of PhCs to control the dispersive properties of photons has established a link with metamaterials. Negative refraction and flat lenses have hence been demonstrated at near-infrared frequency by the use of properly designed PhCs.

To understand the physical principles hidden behind these novel applications, we need to introduce the basic concepts of electromagnetic wave propagation in periodic structures. The origin of the properties of PhCs will be explained by their surface dispersion. A new optical parameter called the curvature index will be introduced to explain how PhCs can stop light diffraction or focus optical signals.

### 1.2.1. *Basic concepts on electromagnetic waves in 2D PhCs*

From the electromagnetic point of view, the optical properties of PhCs are obtained solving an eigenvalue problem based on the resolution of Maxwell equations without any sources. A 2D PhC is depicted by its unit cell which periodically repeats in the directions defined by the basis vectors **a** and **b**.

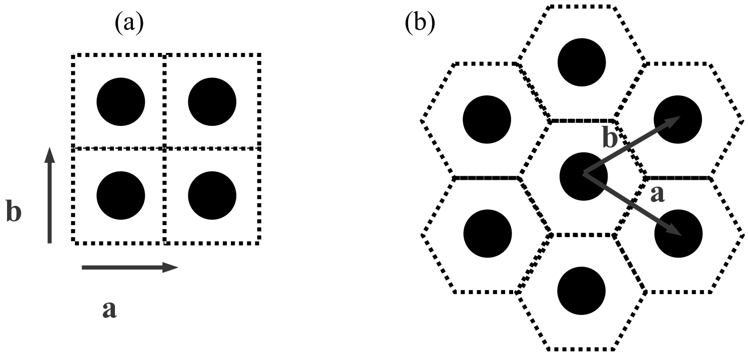


**Figure 1.1.** *Direct lattices for (a) a square lattice, (b) a hexagonal lattice*

For dielectric PhCs, this is summarized in the permittivity function that satisfies:

$$\varepsilon(\mathbf{r} + \mathbf{T}) = \varepsilon(\mathbf{r}) \qquad [1.1]$$

where **T** is the lattice vector defined by $\mathbf{T} = m\mathbf{a} + n\mathbf{b}$, and $m$ and $n$ are integers; see Figure 1.1. In the particular case of lossless and non-dispersive dielectric materials, Maxwell equations expressed in terms of electric and magnetic fields read:

$$\begin{aligned} \nabla \times \mathbf{E}(\mathbf{r},t) &= -\mu_0 \frac{\partial \mathbf{H}(\mathbf{r},t)}{\partial t}, \quad \nabla \cdot \left(\varepsilon(\mathbf{r})\mathbf{E}(\mathbf{r},t)\right) = 0 \\ \nabla \times \mathbf{H}(\mathbf{r},t) &= \varepsilon(\mathbf{r}) \frac{\partial \mathbf{E}(\mathbf{r},t)}{\partial t}, \quad \nabla \cdot \mathbf{H}(\mathbf{r},t) = 0 \end{aligned} \qquad [1.2]$$

where free currents and charges are nulls. Photonic band diagrams are obtained by solving these equations in the harmonic domain. The problem reduces in finding the spatial dependence of the fields for a given angular frequency ω:

$$\begin{aligned} \mathbf{E}(\mathbf{r},t) &= \mathbf{E}(\mathbf{r})e^{-i\omega t} \\ \mathbf{H}(\mathbf{r},t) &= \mathbf{H}(\mathbf{r})e^{-i\omega t} \end{aligned} \qquad [1.3]$$

By introducing this harmonic time dependence in equation [1.2], we obtain two wave equations for the electric field

$$\frac{1}{\varepsilon(\mathbf{r})} \nabla \times \nabla \times \mathbf{E}(\mathbf{r}) = \left(\frac{\omega}{c}\right)^2 \mathbf{E}(\mathbf{r}) \qquad [1.4]$$

and the magnetic field

$$\nabla \times \left( \frac{1}{\varepsilon(\mathbf{r})} \nabla \times \mathbf{H}(\mathbf{r}) \right) = \left(\frac{\omega}{c}\right)^2 \mathbf{H}(\mathbf{r}) \qquad [1.5]$$

It can be proven that the latter equation is an eigenvalue problem characterized by a Hermitian operator $\Xi = \nabla \times \frac{1}{\varepsilon(\mathbf{r})} \nabla \times$, eigenvectors $\mathbf{H}(\mathbf{r})$ and real eigenvalues $(\omega / c)^2$. The expansion of this operator on a Floquet-Bloch basis allows us to numerically solve equation [1.5]. For a given wavevector **k**, the electromagnetic waves called Bloch modes are decomposed into the product of a periodic function $\mathbf{u}_\mathbf{k}(\mathbf{r})$ by a plane wave $e^{i\mathbf{kr}}$:

$$\mathbf{H}_\mathbf{k}(\mathbf{r}) = \mathbf{u}_\mathbf{k}(\mathbf{r})e^{i\mathbf{kr}} . \qquad [1.6]$$

Introducing the expression of $\mathbf{H}_{\mathbf{k}}(\mathbf{r})$ in equation [1.5] gives the equivalent eigenvalue problem:

$$\Theta \mathbf{u}_k(\mathbf{r}) = \left(\frac{\omega}{c}\right)^2 \mathbf{u}_k(\mathbf{r}) \qquad [1.7]$$

with $\Theta_{\mathbf{k}} = (i\mathbf{k} + \nabla) \times \frac{1}{\varepsilon(\mathbf{r})} \times (i\mathbf{k} + \nabla) \times$ the new Hermitian operator that depends on $\mathbf{k}$. The resolution of equation [1.7] for a set of wavevectors gives the photonic dispersion diagram ω(**k**). Due to the periodicity of PhCs, this dispersion relationship is also periodic in the wavevector space: ω(**k**+**G**)= ω(**k**). The reciprocal lattice vector **G** is linked with the lattice vector by $\mathbf{T}.\mathbf{G} = 2\pi$. This definition allows us to define the reciprocal basis (**a***,**b***) and the Brillouin zones. Figure 1.2 shows the first two Brillouin zones for square and hexagonal lattices and Table 1.1 summarizes the direct and reciprocal lattice vectors for square and hexagonal cells consisting of cylinders of radius *r* spaced at a distance *a*.

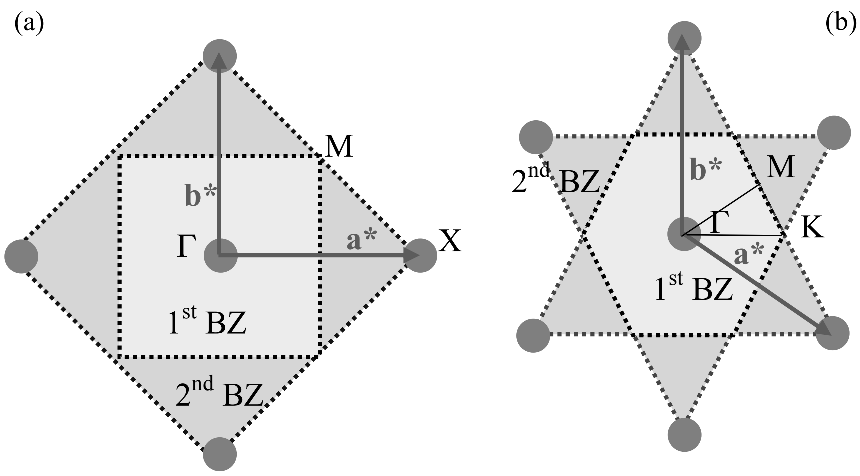


**Figure 1.2.** *First and second Brillouin for (a) square and (b) hexagonal lattices. For a color version of this figure, see www.iste.co.uk/vanbesien/nanophotonics.zip*

It is commonly assumed that all dispersive properties such as the propagation direction or light velocity are retrieved from the dispersion diagram represented in the first Brillouin zone. This mathematical truth must however be analyzed through the physicist's eyes to catch the real behavior of electromagnetic waves. Negative refraction in PhCs in particular must be analyzed carefully to avoid misconception with the optical properties of metamaterials.

In practice, several methods allow us to numerically solve equation [1.5] for 2D or 3D PhCs. To our knowledge, the most efficient method was developed by S.G. Johnson. A code called MPB, for MIT Photonic-Band, can be freely downloaded at http://ab-initio.mit.edu/wiki/index.php/MIT_Photonic_Bands.

| | **Square lattice** | **Hexagonal lattice** |
|---|---|---|
| **Direct lattice vectors** | $\mathbf{a} : a(1,0)$<br>$\mathbf{b} : a(0,1)$ | $\mathbf{a} : a(1,0)$<br>$\mathbf{b} : a(1/2, \sqrt{3}/2)$ |
| **Reciprocal lattice vectors** | $\mathbf{a}^* : \frac{2\pi}{a}(1,0)$<br>$\mathbf{b}^* : \frac{2\pi}{a}(0,1)$ | $\mathbf{a}^* : \frac{2\pi}{a}(1,-1/\sqrt{3})$<br>$\mathbf{b}^* : \frac{2\pi}{a}(0,2/\sqrt{3})$ |
| **Filling factor** | $f = \pi \frac{r^2}{a^2}$ | $f = \frac{2\pi}{\sqrt{3}} \frac{r^2}{a^2}$ |

**Table 1.1.** *Direct and reciprocal basis vectors for square and hexagonal lattices*

### 1.2.2. *Dispersion surfaces, equi-frequency curves and group velocity*

The power of PhCs to mold the flow of light lies in the richness of their dispersion relationship. To illustrate this purpose, we begin with a 2D PhC made of air holes of radius $r=0.3a$ settled in a square lattice and etched in a dielectric semiconductor of refraction index $n=3$. Since our problem is two-dimensional, two polarization cases, TE (transverse-electric) or TM (transverse-magnetic), can be distinguished. For TE polarization, the unique non-null component of the magnetic field is perpendicular to the propagation plan (i.e. in the z-direction). The dispersion diagram computed with MPB is plotted for TE polarization for **k**-vectors lying in the 1st Brillouin zone; see Figure 1.3.

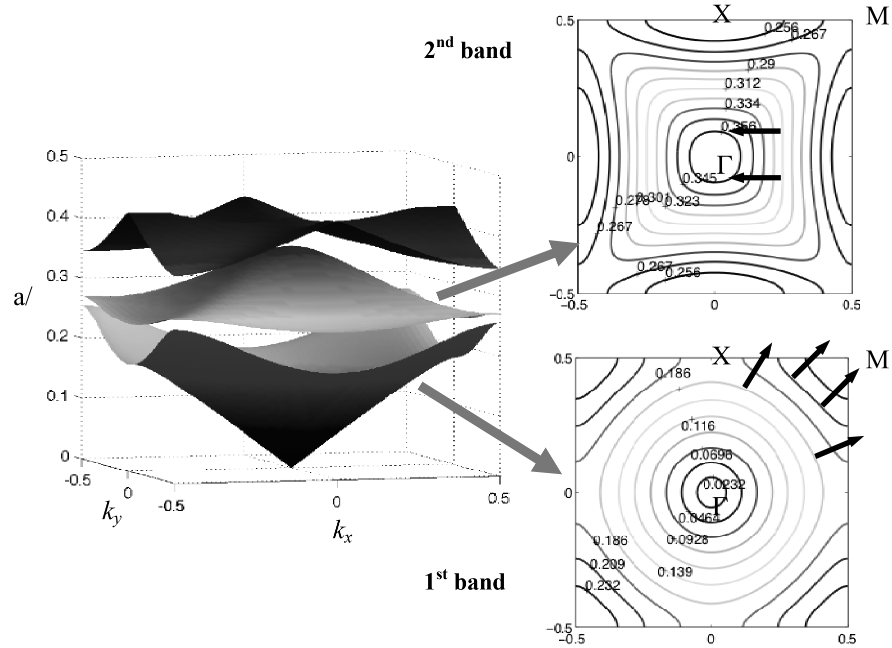


**Figure 1.3.** *Dispersion surfaces and equi-frequency curves of the 1st and 2nd bands for a square lattice of air holes (radius r/a=0.3) in a dielectric material of optical index 3. The black arrows indicate the direction of the group velocity. For a color version of this figure, see www.iste.co.uk/vanbesien/nanophotonics.zip*

This dispersion diagram is plotted for a normalized frequency $u = a / \lambda$ and for wavevectors $(k_x, k_y)$ expressed in units of $2\pi / a$. Let us plot the equi-frequency curves of the first and second bands, i.e. curves defined by the set of $(k_x, k_y)$ coordinates obtained for a fixed frequency; see Figure 1.3. Starting from low frequencies, rounded equi-frequency curves (EFCs) flatten around *u=0.2*. In the ΓM direction, the EFCs are rounded again but with opposite curvatures. For the second band, an opposite behavior is observed and almost circular EFCs are seen around *u=0.33*. This variety of EFC is at the origin of the interest in PhCs for beam steering and shaping operations. Bloch modes in fact follow a propagation direction determined by their group velocity. The group velocity is linked to the direction of the electromagnetic energy flow and can be determined directly from the dispersion surfaces with:

$$\mathbf{v}_{\mathbf{g}} = \nabla_{\mathbf{k}}\omega(\mathbf{k})\,. \qquad [1.8]$$

The group velocity is therefore perpendicular to the EFCs since it derives from the gradient of the dispersion surfaces; see Figure 1.3.

## 1.3. Fundamental dispersion effects

Three main ultra-refraction effects have emerged from the particular shapes of the PhC dispersion curves. Let us now introduce important tools and rules to predict light refraction at PhC interfaces and the behavior of beams in these highly dispersive media.

### 1.3.1. *The construction line method*

The construction line method allows us to determine the direction of a beam from the dispersion curves of a medium. To understand this method, consider two homogeneous media of refraction index $n_1$ and $n_2$. The Snell-Descartes law, $n_1 \sin\theta_1 = n_2 \sin\theta_2$, is known to give the propagation direction of an incident wave refracted at an interface separating two homogeneous media. It is interesting to interpret this formula in the framework of the EFC diagrams. For that purpose, multiply the left and right terms of the Snell-Descartes law by $2\pi / \lambda$ to obtain the continuity of the transverse wavevectors of the incident and refracted waves: $k_t^{(1)} = k_t^{(2)}$. For the equi-frequency diagrams associated with each media, this consists of plotting a line parallel to the normal direction at a distance $k_t^{(1)}$ from the origin; see Figure 1.4. Two intersection points are obtained between the EFCs and the construction line for each medium. For the first medium, points A and B are associated with the incident and reflected waves respectively. In the second medium, points C and D are possible solutions. However, owing to the conservation of the energy flow, only point C can be associated with the refracted waves. Because no incident wave is considered in the second medium, point D does not represent a physical solution. Let us note that because of the homogeneity of the media, the associated group velocities and wavevectors are parallel. Finally, the refraction angle determined by the Snell-Descartes law is retrieved with the EFC diagram.

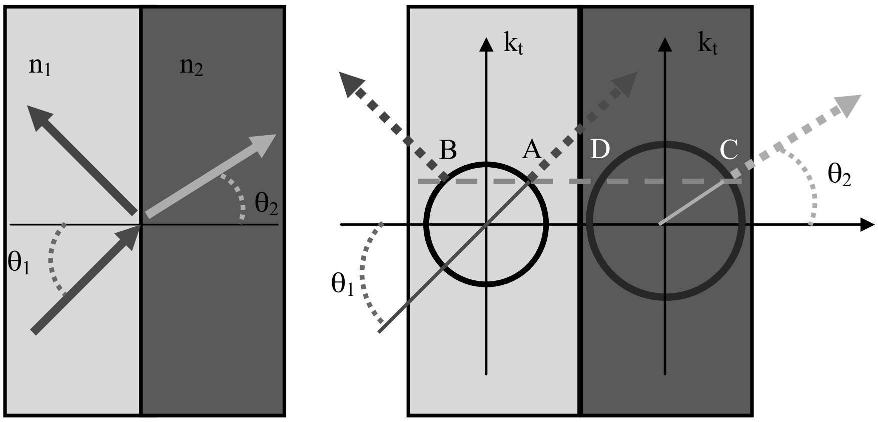


**Figure 1.4.** *Refraction of light at the interface of two homogeneous media of indices $n_1$ and $n_2$ ($n_2$>$n_1$). The arrows indicate the direction of the energy flow and of the group velocity. The dashed lines correspond to the construction lines. For a color version of this figure, see www.iste.co.uk/vanbesien/nanophotonics.zip*

The same method applies when the second media is a PhC. However, when the frequency is sufficiently large, several diffraction orders can open, leading to multiple refracted waves. This property can again be captured with the EFC diagram, but the PhC wavevector has to be replaced by $\mathrm{k}^{(2)} + \mathrm{G}$. The transverse wavevector continuity is now written $k_t^{(2)} = k_t^{(1)} + n\dfrac{2\pi}{a_t}$, where $a_t$ is the transverse periodicity of the crystal and $n$ an integer. Finally, this last equation can also read like the grating formula $\sin\theta_n = \sin\theta_1 + n\dfrac{\lambda}{a_t}$ where $\theta_n$ are the refracted angles.

### 1.3.2. *A beam propagation model*

Ultra-refraction effects are revealed when beams are launched into photonic crystals. It is therefore important to quantify the behavior of such beams when they propagate inside highly dispersive materials. For that purpose, we introduce a beam propagation model that captures the diffraction process through the concept of the curvature index.

Consider a Gaussian beam of waist $W_0$ propagating in the y-direction. At the origin, for y=0, the normalized field is $U(x,y)=e^{-\frac{x^2}{W_0^2}}$. This Gaussian beam has to be decomposed into a continuous set of Bloch modes inside the PhC. To catch the essential behavior of the beam, let us assume that the Gaussian beam may be decomposed into a simple basis of plane waves. This slowly varying envelope approximation consists of neglecting the rapid oscillations of the field at the lattice period scale. With these approximations the Gaussian beam reads:

$$U(x,y)=\int_{-\infty}^{+\infty} A(k_x)e^{ik_x x+ik_y(k_x)y}dk_x \,. \qquad [1.9]$$

At a given frequency ω, the function $k_y(k_x)$ describes the corresponding EFC and $A(k_x)=e^{-k_x^2/(W_0/2)^2}$ is the spectral distribution of the Gaussian beam. In the case of normal incidence (centered around $k_x$=0), the Taylor expansion at the second order gives:

$$k_y(k_x)=k_y(0)+k_x\left.\frac{\partial k_y}{\partial k_x}\right|_{k_x=0}+\frac{k_x^2}{2}\left.\frac{\partial^2 k_y}{\partial k_x^2}\right|_{k_x=0} \,. \qquad [1.10]$$

Assuming that the y-axis points to a high symmetry direction of the lattice and because of the parity of the function $k_y(k_x)$ this polynomial expansion becomes:

$$k_y(k_x)=k_y^{(0)}+\frac{k_x^2}{2}\left.\frac{\partial^2 k_y}{\partial k_x^2}\right|_{k_x=0} \,, \qquad [1.11]$$

where $k_y^{(0)}=k_y(0)$. For a homogeneous medium, the second derivative depends on the wave number $k_0=2\pi/\lambda$ and the optical index *n*: $\left.\frac{\partial^2 k_y}{\partial k_x^2}\right|_{k_x=0}=-\frac{1}{k_0 n}$. By analogy with the homogenous medium, we define the curvature index $n_c$:

$$n_c=-\frac{1}{k_0}\left(\left.\frac{\partial^2 k_y}{\partial k_x^2}\right|_{k_x=0}\right)^{-1} \,. \qquad [1.12]$$

The curvature of the EFCs is then related to the curvature radius $k_0 n_c$ and any EFC is approximated by a parabolic one for $k_x \ll k_0$:

$$k_y(k_x) = k_y^{(0)} - \frac{k_x^2}{2}\frac{1}{k_0 n_c}, \qquad [1.13]$$

which can be recognized as the paraxial approximation used to derive the analytical evolution of a Gaussian beam propagating in a homogeneous medium. However, to take into account that the beam propagates into a PhC, the optical index is replaced by the curvature index. With this formulation, equation [1.9] becomes:

$$U(x,y) = e^{ik_y^{(0)}y} \int_{-\infty}^{+\infty} A(k_x) e^{ik_x x - i\frac{k_x^2}{2k_0 n_c}y} dk_x \,. \qquad [1.14]$$

This Gauss integral can be solved analytically, and the beam reads:

$$U(x,y) = \frac{W_0}{w(y)} e^{-x^2/W(y)^2} e^{ik_y^{(0)}y} e^{i\phi(x,y)}, \qquad [1.15]$$

where $W(y)$ is the waist of the beam at the propagation distance $y$ and $\phi(x,y)$ is a phase function:

$$\begin{aligned} W(y) &= W_0 \sqrt{1 + \frac{4}{W_0^2}\left(\frac{y}{k_0 n_c}\right)^2} \\ \phi(x,y) &= -\frac{x^2 y}{n_c W(y)^2} \end{aligned}, \qquad [1.16]$$

Formulation [1.16] of the beam waist in terms of the local curvature of the EFCs highlights numerous beam-shaping effects. In homogeneous media, for example, light diffraction is related to the refractive index $n$ that defined the local curvature radius of the circular EFCs. At a long distance, the beam waist increases with a linear law $2y/(W_0 k_0 n)$. The next section will demonstrate that for PhCs one can play with the EFC curvature to suppress light diffraction.

### 1.3.3. *The self-collimation effect*

As shown previously, Gaussian beams suffer from diffraction when they propagate in homogeneous media, which leads to an irreversible beam spreading. In common optical systems this effect is combatted by the use of optical waveguides that confine light in the transverse direction. This strategy always requires nano- or micro-structure semiconductors to create an area where optical signals are trapped by index guiding or band gap effects such as in PhC waveguides. Another way to suppress light diffraction is to use a nonlinear effect such as the self-focusing effect in Kerr media. However, in that case, laser sources of strong intensity are required because of the weak nonlinear response of semiconductors, which does not facilitate their integration in future integrated optical devices. H. Kosaka proposed an alternative approach in 1999 that stemmed from the linear optical properties of PhCs. He showed that properly designed PhCs sustain diffraction-free beams without the use of optical waveguides or nonlinear effects. The self-collimation effect appears in 2D or 3D PhCs and has attracted much attention over recent decades in particular because of the simplicity of the structures involved. Since the self-collimation effect is obtained without breaking the lattice symmetry of PhCs, no specific alignment with the source is needed. In addition, PhC membranes working below the light line allow the propagation of self-collimated beams at the millimeter scale with reduced optical losses.

To understand the self-collimation effect, let us take a closer look at the EFCs computed for a square lattice of air holes etched into a semiconductor depicted in Figure 1.5. For the first dispersion band, flat EFCs appear in the ΓM direction around the reduced frequency $a/\lambda$=0.22. At lower frequencies, the EFCs present a positive curvature, while for higher ones the sign of the curvature becomes negative. The impact of negative values for the curvature index will be discussed in detail in the following sections. Following on from the previous section, the curvature index can be derived and shows a Fano-like shape around the self-collimation frequency. The self-collimation frequency is then associated with an infinite curvature index (or a null value of the curvature $1/n_c$ ).

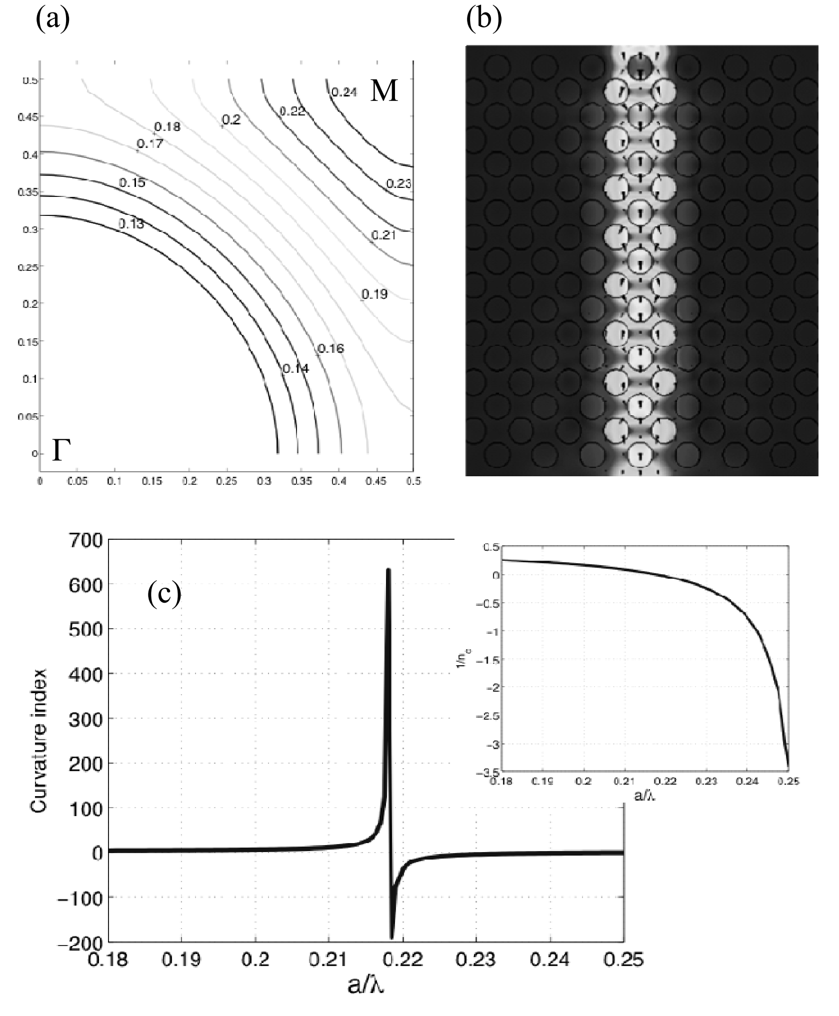


**Figure 1.5.** *(a) EFCs for the 1st band of a square lattice in TE polarization. (b) Simulation of a Gaussian beam propagating in the self-collimation regime. (c) Variation of the curvature index with respect the reduced frequency. The inset shows the variation of* $1/n_c$ *. For a color version of this figure, see www.iste.co.uk/vanbesien/nanophotonics.zip*

This criterion allows us to define the self-collimation frequency precisely (equal to 0.217 in this case) which is less subjective than the denomination “flat EFC”. The analytical formulation of the beam waist (equation [1.16]) also shows that in an indefinite PhC, the beam keeps a constant waist $W_0$ when $1/n_c = 0$, which is consistent with the definition of a self-collimated beam.

The self-collimation effect can also appear at higher frequencies for other dispersion surfaces. As shown in Figure 1.3, “flat EFCs” are also present in the second band around the reduced frequency 0.31, but this time in the ΓX direction of the square lattice. The particular interest in working with the first band stems from the possibility of propagating a guided self-collimated beam in a PhC membrane since the self-collimation frequency is below the light line. This property has been exhibited in the experimental work of Rakich and co-authors. Several studies have, in addition, demonstrated that basic optical functions such as wavelength filters or beam splitters can be designed with PhCs operating in the self-collimation regime. Polarization-independent self-collimated beams have also been predicted in appropriate structures. However, it is worth mentioning that little experimental research has been carried out compared with the photonic crystal waveguide approach.

### 1.3.4. *Mesoscopic self-collimation of light*

As seen previously, diffraction is cancelled in PhC when EFCs of zero-curvature are utilized. Another way to obtain self-collimation has recently been shown with more complex structures based on PhC properties. These devices, called PhC superlattices, involve a periodic set of PhC slabs stacked with unpatterned dielectric layers. These structures emerge with the concept of zero-average index metamaterials and the first experimental proof of the propagation of self-colllimated beams was made by Mocella and co-authors. This effect, called “mesoscopic self-collimation”, has been explained in terms of a refocalization mechanism that exactly compensates light diffraction at the mesoscopic scale (i.e at tens of lattice periods). This approach enables the design of structures presenting an extremely small filling factor in air holes. Arlandis and co-authors have in addition shown that slow light and the self-collimation effect can simultaneously be combined, a property unattainable in common 2D PhCs.

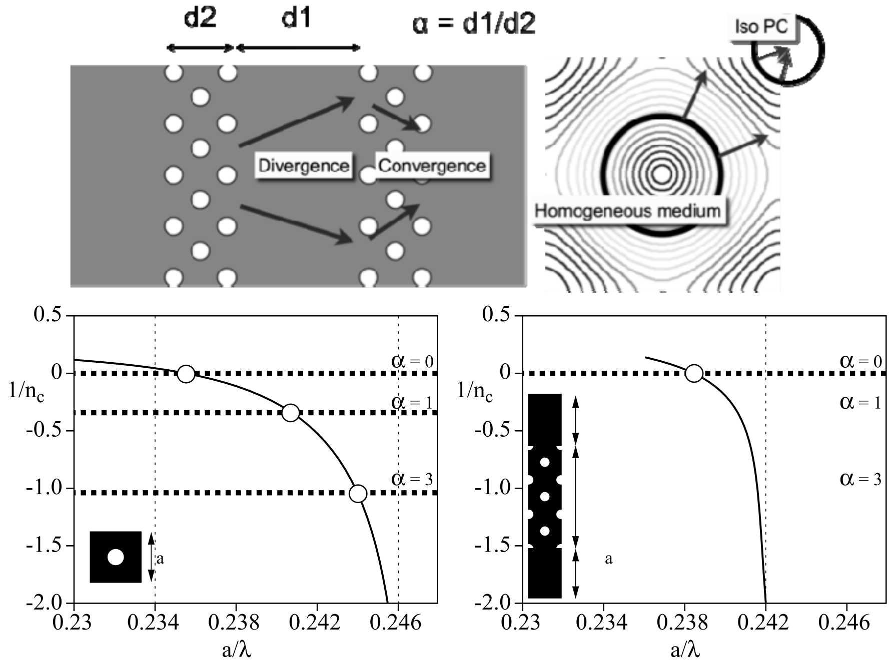


**Figure 1.6.** *Schematic representation of a PhC superlattice. The PhC layer exactly compensates for diffraction in the homogeneous layer. This is possible when the PhC slab operates in a focalization regime where the curvature index is negative. (a-b) Curvature function 1/nc computed in ΓM direction versus the reduce frequency. (a) For the infinite 2D PhC of unit cell depicted in the inset. The intersection points between 1/nc and the straight dashed lines for α = 0, 1 and 3 correspond to the self-collimation frequencies for the unbounded 2D PhC and for PhC superlattices of two filling ratios in PhC layers respectively. (b) Graph of $1/n_c$ computed for the supercell corresponding to a PhC superlattice with α = 1 and $d_1 = 3a\sqrt{2}$ shown in the inset. For a color version of this figure, see www.iste.co.uk/vanbesien/nanophotonics.zip*

The mesoscopic self-collimation effect is explained in the framework of the beam propagation model developed in section 1.3.2. These structures resemble Bragg mirrors where some homogeneous layers are replaced by PhC slabs of thickness $d_2$. These slabs are stacked with homogeneous layers (air or semiconductor materials) of thickness $d_1$ and optical index $n_1$; see Figure 1.6. Assuming that reflection can be neglected, the Gaussian beam after one macro-period $D = d_1 + d_2$ reads:

$$U(x,D) = \int_{-\infty}^{+\infty} A(k_x) e^{ik_y^{(1)}(k_x)d_1} e^{ik_y^{(2)}(k_x)d_2} e^{ik_x x} dk_x \ , \qquad [1.17]$$

where $k_y^{(1)}(k_x)$ and $k_y^{(2)}(k_x)$ are the wavevectors in the propagation direction for the PhC and homogeneous layers respectively. Plugging the Taylor expansion [1.13] of $k_y^{(1)}(k_x)$ and $k_y^{(2)}(k_x)$ into equation [1.17], we obtain the formula:

$$U(x,D) = e^{i\overline{k}_y^{(0)} D} \int_{-\infty}^{+\infty} A(k_x) e^{ik_x x - i\frac{k_x^2}{2k_0 \overline{n}_c} D} dk_x \ . \qquad [1.18]$$

The term $\overline{k}_y^{(0)} = (k_y^{(1)} d_1 + k_y^{(2)} d_2)/D$ represents the mean phase and $\overline{n}_c$ is the average curvature index defined by: $\frac{1}{\overline{n}_c} = \frac{1}{D}\left(\frac{d_1}{n_c^{(1)}} + \frac{d_2}{n_c^{(2)}}\right)$. In the homogeneous layer, the curvature index is reduced simply to the refractive index $n_c^{(1)} = n_1$ while $n_c^{(2)}$ has to be numerically computed for a given PhC. Finally, after a macro-period distance the beam waist is $W(D) = W_0 \sqrt{1 + \frac{4}{W_0^2}\left(\frac{D}{k_0 \overline{n}_c}\right)^2}$. This analysis allows us to predict that mesoscopic self-collimated beams propagate when the mean curvature index is infinite. This condition is satisfied when the PhC slab operates at a frequency where $n_c^{(2)}$ is negative and only depends on the ratio $\alpha$=d1/d2:

$$\frac{1}{n_c^{(2)}} = -\frac{\alpha}{n_1} \ . \qquad [1.19]$$

The last equation shows that the mesoscopic self-collimation frequency can be tuned by varying the ratio of the slab thicknesses. For example, for a square lattice of air holes (of radius r/a=0.20) etched into a semiconductor of index $n_1 = 2.9$, the self-collimation frequencies predicted by the beam propagation model are 0.239 and 0.243 for $\alpha$=1 and $\alpha$=3 respectively. This result is confirmed by the direct computation of the dispersive properties of the PhC superlattice, which shows that self-collimation is reached at the reduced frequency 0.239 for equal PhC and homogeneous slab thicknesses; Figure 1.6. Note that the filling factor in air is dramatically reduced since it attains only 3% for $\alpha$=3. Another particular property concerns the scale invariance of the mesoscopic self-collimation effect. The condition described in equation [1.19] shows that the operating frequency is insensitive to the size of the macro-period D. However, the photonic band gap induced by this Bragg mirror-like device instead depends on D. This is shown in Figure 1.7, where the dispersion curves in the propagation direction and the associated group index $n_g = c / v_g$ are represented for a fixed α = 1 and for two macro-periods.

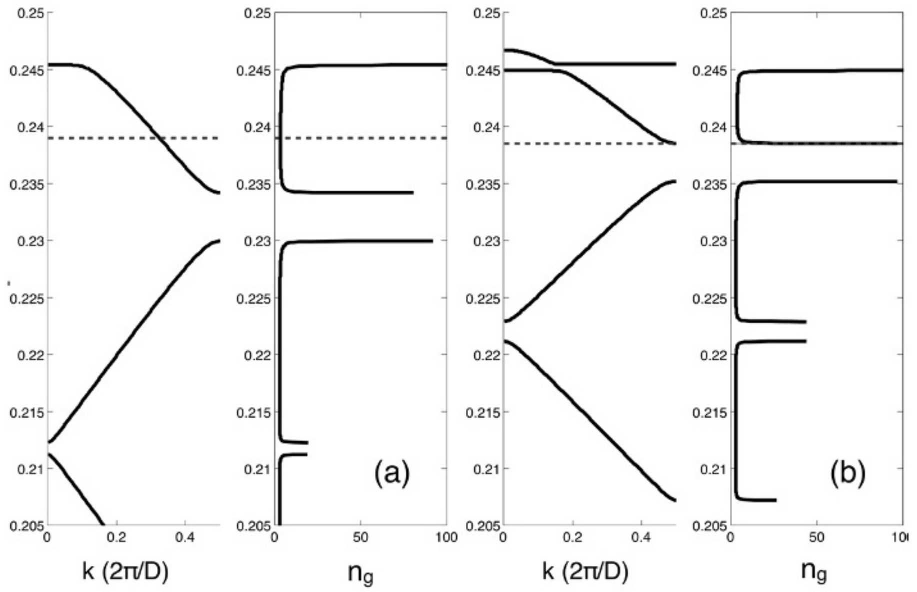


**Figure 1.7.** *Band diagram in the ΓM direction and group index of the PhC superlattice for α = 1. The dashed lines indicate the self-collimation frequency a/λ = 0.239. (a) The macro-period is* $D = 6a\sqrt{2}$ *. (b) The macro-period is* $D = 8a\sqrt{2}$ *. In that case the self-collimation effect appears in the slow light regime*

New photonic band gaps originating from Bragg interferences open in the frequency range corresponding to the transparent window of the unbounded 2D PhC. It is seen that an additional forbidden band appears at the vicinity of the mesoscopic self-collimation frequency for $D = 8a\sqrt{2}$ . In that case, high group indexes of 30 to 50 are found in the self-collimation regime. This property never appears in common 2D PhCs since the self-collimation frequency is always set far from the band gap edge. Finally, FDTD simulations demonstrate that PhC superlattices sustain self-collimated beams over a length of 1000a; see Figure 1.8.

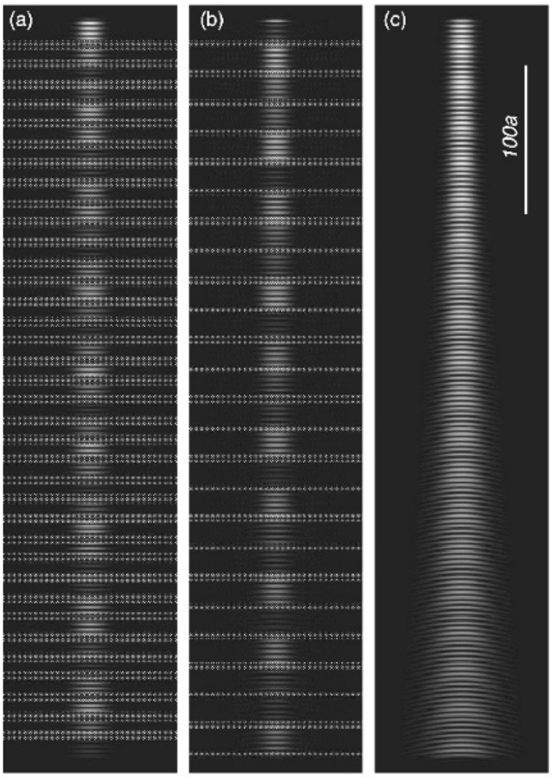


**Figure 1.8.** *FDTD simulation of the propagation of Gaussian beams of waist $W_0$= 8a. (a) At the reduced frequency a/λ = 0.239 for a PhC superlattice for* $d_1 = 4a\sqrt{2}$ *and α = 1. (b) At the reduced frequency 0.243 for* $d_1 = 3a\sqrt{2}$ *and α = 3. (c) The same Gaussian beam propagating in a homogeneous medium of optical index 2.9 and for a/λ = 0.239. For a color version of this figure, see www.iste.co.uk/vanbesien/nanophotonics.zip*

In conclusion, self-collimation of light in linear photonic crystals is a fascinating optical effect that provides an alternative approach to the common waveguide solution. It is based on the unique dispersive property of periodic media and can provide new solutions for future integrated optical chips.

### 1.3.5. *The superprism effect*

The superprism effect can be seen at the first level as the opposite to the self-collimation effect. In the self-collimation regime, all the incident waves are forced to follow the same propagation direction. The superprism effect stems, on the contrary, from an ultra-sensitivity of the light path with respect to the incident angle or the wavelength. A photonic crystal slab can be similar to a prism that separates the color of light but with an enhanced separation power. This discovery, again attributed to H. Kosaka, has led to intense research activity around the world owing to the possibility of realizing the wavelength division functionality in miniaturized devices.

The origin of the superprism effect is again understood with the analysis of EFCs obtained for 2D PhCs. Take the previous example of a square lattice of air holes (r/a=0.30) drilled into a dielectric substrate of refractive index 3. For TE polarization, sharp EFCs appear in the ΓX direction for the second dispersion surface; see Figure 1.9. Around this angular area, for a fixed frequency, the direction of the group velocity drastically changes when the transverse wavevector $\Delta k_{\perp} = k_0(\sin\theta_B - \sin\theta_A)$ (with $k_0 = 2\pi/\lambda$) varies. We obtain the angular superprism effect since this modification is driven by the incident angle. In the case described in Figure 1.9, a small variation of the incident angle $\delta\theta_i$, less than 10°, produces a huge deflection angle $\delta\theta_c$ of 45°. Point B in fact corresponds to the limit incident angle for which the propagation direction is parallel to the interface. In the same way, for a fixed incident angle and for a small variation of the frequency, i.e. along the given light line, the orientation of group velocity may undergo a large shift leading to the frequency superprism effect. Two parameters $p$ and $q$ are usually introduced to measure the variation of the deflection angle versus the variation of the incident angle or the frequency:

$$p = \left.\frac{\partial\theta_c}{\partial\theta_i}\right|_{\omega} ; \quad q = \left.\frac{\partial\theta_c}{\partial\omega}\right|_{\theta_i} . \qquad [1.20]$$

These parameters can be derived directly from the dispersion relationship of the PhC and allow optimization of compact spectrometers or wavelength demultiplexers based on PhCs.

An efficient PhC for superprism operation has to provide EFCs of high local curvature. However, the beam propagation model shows that high curvature (or a small curvature index) leads to the spread of the initial beam. This amplified diffraction degrades the performances of the optical devices based on the superprism effect since several beams can overlap at the end of the structure. This effect decreases the resolution of the spectrometer and increases the crosstalk for wavelength division operation.

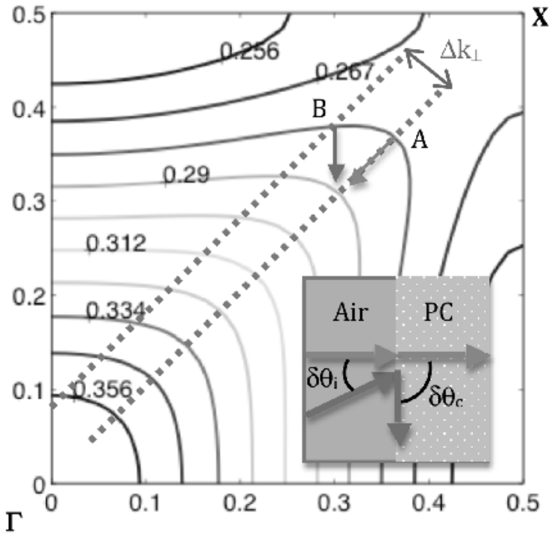


**Figure 1.9.** *EFCs of the 2nd band for a square lattice of air holes in TE polarization. The arrows indicate the group velocities at points A and B. The construction lines (dashed lines) are plotted for normal and oblique incidences. The inset represents the direction of a beam for incident angles corresponding to points A and B. For a color version of this figure, see www.iste.co.uk/vanbesien/nanophotonics.zip*

Finally, E. Cassan found a compromise between large deflection and low diffraction by mixing both the superprism and self-collimation effect. Graded photonic crystals, described in Chapter 3, may also be an elegant solution to managing both the self-collimation and beam steering effects.

### 1.3.6. *Negative refraction and -1 effective index in photonic crystals and metamaterials*

The Snell-Descartes law is known to govern light refraction at the interface of two transparent materials of optical indices $n_1$ and $n_2$. The refraction and incident angles are linked by the well-known formula $n_1 \sin\theta_1 = n_2 \sin\theta_2$. Transparent materials that are available in nature present positive optical indices so that the refraction angle is always positive. With the advancement of metamaterials, this result has been reconsidered, for instance, with the experimental demonstration of negative refraction. These manmade materials present a periodic set of metallic resonators and behave in the long wavelength limit (i.e when the $\lambda$ is at least ten times larger than the periodic structuration) as homogeneous media of both negative electric and magnetic permittivities. The concept of negative index metamaterials emerged during the 2000s and led us to revisit conventional optical effects, some of which had been described by Veselago in 1968. Among them, the flat lenses allowing optical super-resolution proposed by J.B. Pendry have attracted much attention. However, the realization of such devices operating at optical wavelengths is still a great challenge because of the technological problems related to the miniaturization of metamaterials and to their high optical losses. To circumvent these issues, the dielectric approach with the use of PhC has been experimented with by several groups. The concept and experimental results concerning flat lenses based on the properties of 2D PhCs will be detailed in Chapter 2. In the long wavelength limit, similar homogenization approaches used for metamaterials have demonstrated that negative refraction in PhCs originates from electric and magnetic resonances that induce both negative effective permittivity and permeability. However, in the diffraction regime where the wavelength is comparable to the lattice period, homogenization techniques fall down. Up until now, it has seemed difficult to evaluate the effective permittivity and permeability, even if some results have shown that some fundamental properties persist between the homogenization and the diffraction regimes. Despite this fundamental problem, negative refraction in PhC can also be understood with the analysis of EFCs. However, several levels of interpretation are required to catch the real physics behind negative refraction in PhCs.

*A. Negative refraction in metamaterials*

Let us recall the essential physics of electromagnetic waves in metamaterials presenting both negative ε and μ. In the harmonic regime, similarly to conventional positive index material, the basic propagation solution is the plane wave: $U(\mathbf{r},t)=e^{i\omega t}e^{-i\mathbf{kr}}$. In that case, the operator Nabla reads in its simplest form: $\nabla=-i\mathbf{kr}$. Plugging this into Maxwell equations, we obtain the following formulas:

$$\begin{aligned}\mathbf{k}\times\mathbf{E}&=\omega\mu\mathbf{H}\\ \mathbf{k}\times\mathbf{H}&=-\omega\varepsilon\mathbf{E}\end{aligned}. \qquad [1.21]$$

These identities commonly stem from the fact that in a common medium presenting double positive ε and μ, (**E**, **H**, **k**) forms a direct trihedron. Equation [1.21] shows that this right-handed wave transforms into a left-handed wave in double negative medium (i.e for ε<0 and μ<0). The calculation of the Poynting vector gives $\mathbf{P}=\frac{H^2}{2\omega\varepsilon}\mathbf{k}=\frac{E^2}{2\omega\mu}\mathbf{k}$, showing that the energy flow is opposite to the wavevector **k**. As a consequence, negative refraction index metamaterials support strange electromagnetic waves of opposite phase and group velocities. This singularity explains why a beam is refracted in the "wrong" direction at the interface of a negative index metamaterial. The construction line method shows that the continuity of the incident energy flow through the interface is ensured when the refracted beam corresponds to point D; see Figure 1.10. For this point presenting opposite phase and group velocities, the refracted angle is negative. *Finally, negative refraction originates from the left-handed character of electromagnetic waves in negative index metamaterials.*

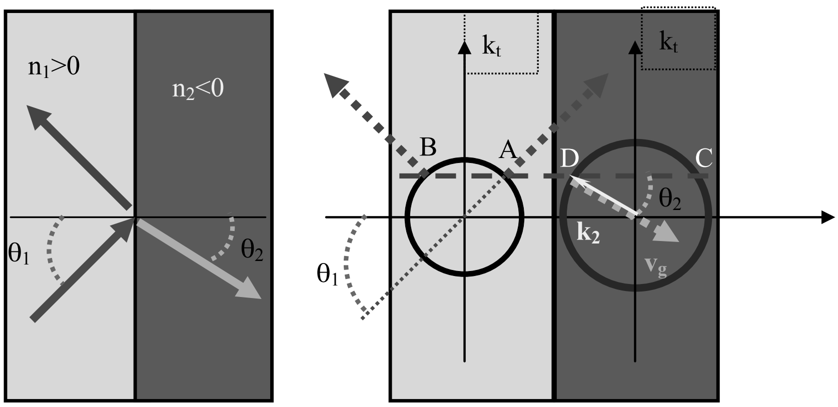


**Figure 1.10.** *Light refraction at the interface of right-handed ($n_1>0$) and left-handed ($n_2<0$) homogeneous media. The arrows indicate the direction of the group velocity. Inside the left-handed media, the wavevector $\boldsymbol{k_2}$ and the group velocity are opposite. For a color version of this figure, see www.iste.co.uk/vanbesien/nanophotonics.zip*

*B. Negative refraction in photonic crystals*

Photonic crystals are recognized to mimic some optical properties of metamaterials. They are able in particular to negatively refract Gaussian beams or to focus light as for metamaterial lenses. This has led to false ideas being peddled about the real physics at work in PhC devices. A clear understanding of the origin of negative refraction in PhCs is nevertheless necessary to catch the optical limitations of PhC-based devices such as superlenses.

*B.1. Negative refraction on the first band*

Consider again the previous PhC made of a square lattice of air holes (r/a=0.20). The construction line plotted in Figure 1.11 intersects two points A and B at the reduced frequency 0.16 and 0.20. The associated group velocities are seen to point either side of the construction line leading to a positive refraction at A and a negative one at B. Similarly to the superprism effect, the propagation direction of the refracted beam is dictated by the local curvature of the EFCs. These results, confirmed by FDTD simulations, show that a Gaussian beam launched into the air with an incident angle of 20° is deflected with a negative angle of refraction when its reduced frequency is 0.20; see Figure 1.11. We also remark that in the first band, negative refraction holds until the scalar product of the phase and group velocities is positive: $\mathbf{k}.\mathbf{v}_g > 0$ . *Contrary to negative optical index metamaterials, negative refraction in PhCs does not involve left-handed electromagnetic waves, but it instead results from the special shape of EFCs that present a local negative curvature.*

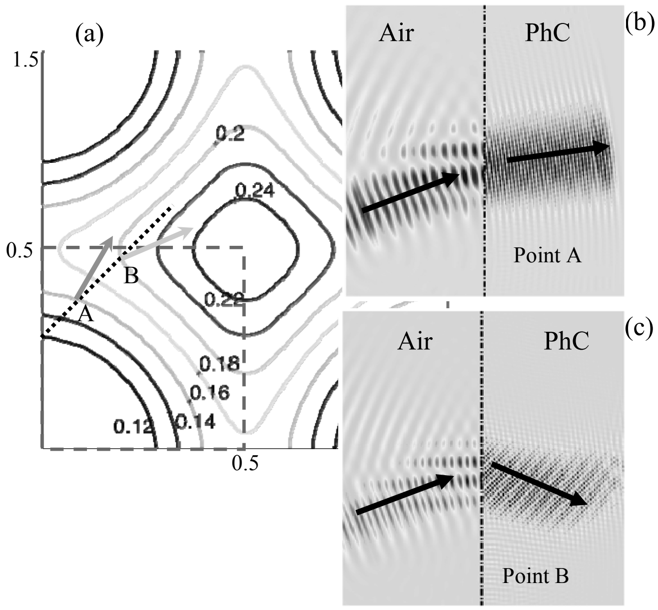


**Figure 1.11.** *(a) EFCs of the 1st band for a square lattice of air holes in TE polarization. The dotted square delimits the 1st Brillouin zone. The arrows indicate the direction of the group velocity. Points A and B correspond to positive and negative refraction cases, respectively. (b-c) FDTD simulations of the refraction of a Gaussian beam between air and PhCs consisting of a square lattice of air holes. The ΓM direction of the lattice corresponds to the y-direction. The incident angle is fixed at 20° but the reduced frequency is 0.16 and 0.20 for (b) and (c) respectively. For a color version of this figure, see www.iste.co.uk/vanbesien/ nanophotonics.zip*

*B. Negative refraction on the second band: do left-handed waves exist in PhCs ?*

In the first band, negative refraction is seen to originate from the negative curvature on EFCs located near the band gap edge. However, let us now consider the second dispersion band for the same square lattice of air holes. In the 1st Brillouin zone, almost circular EFCs are found around the reduced frequency 0.33 and the negative slope of the dispersion relation implies that the group velocity points inward; see Figure 1.12. In that case, we may conclude that the negative scalar product $\mathbf{k}.\mathbf{v_g} < 0$ implies that the corresponding Bloch modes present a left-handed behavior. Similar to the picture in Figure 1.10 for negative index metamaterials, when the EFCs becomes rounded, the dispersion relation is almost isotropic and we can define an effective phase index $n_{eff}$ linking the wavevector and the frequency:

$$k_x^2 + k_y^2 = \left(\frac{\omega}{c}\right)^2 n_{eff}^2 \qquad [1.22]$$

According to the definition of left-handed waves, this effective phase index is negative when the phase and group velocities point in opposite directions. This vision has been largely shared in the photonic crystal community as shown by the works of Foteinopoulo and co-authors, who have used the concept of a negative refraction index to describe PhCs. From these initial works, PhCs have been reduced to particular metamaterials. However, several studies made in 2005 and 2006 have demonstrated that this schematic should be questioned. The Fourier analysis of Bloch modes shows that for the first band, and far from the band gap edge, a fundamental wave propagates almost all the electromagnetic energy. The product of its phase and its group velocity is also always positive ($\mathbf{k.v}_g > 0$) even when the negative refraction regime is reached.

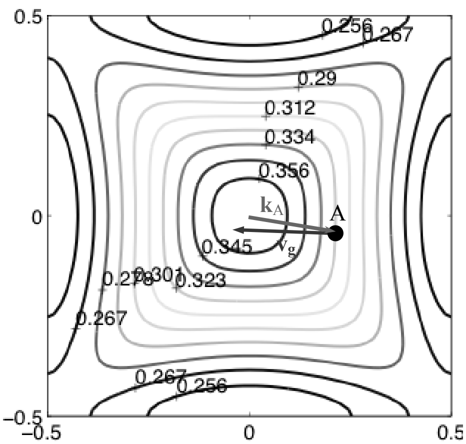


**Figure 1.12.** *EFCs of the 2nd band for a square lattice of air holes in TE polarization. The scalar product of the wavevector and group velocity is negative for all working points in the 1st Brillouin zone. For a color version of this figure, see www.iste.co.uk/vanbesien/nanophotonics.zip*

To understand this counterintuitive result, consider a homogeneous medium such as air and introduce a periodic condition in one direction of space. Due to the band folding, the photon dispersion in air $k = \omega / c$ looks more complicated; see Figure 1.13. If we only consider the 1st Brillouin zone, opposite phase and group velocities appear for each even number of band folding. However, left-handed waves cannot appear in that case since air is a right-handed medium. For example, for point A lying in the 1$^{st}$ Brillouin zone, the wavevector $\mathbf{k_A}$ is opposite the group velocity. This unrealistic result for electromagnetic waves in air becomes possible in the unfolded band diagram by considering the associated point B. In that case, $\mathbf{k_B}$ is the real wavevector associated with a parallel group velocity. Then a clear understanding of the wave property requires us to unfold the dispersion relation observed in the 1$^{st}$ Brillouin zone. As proven by Lombardet and co-authors, this strategy has to be extended for PhCs. Finally, a Bloch wave can be decomposed into a set of waves each of which carry a part of the energy. Far from the band gap edge, a Bloch mode can be assimilated to a unique plane wave whose wavevector and group velocity have to be researched in the unfolded band diagram.

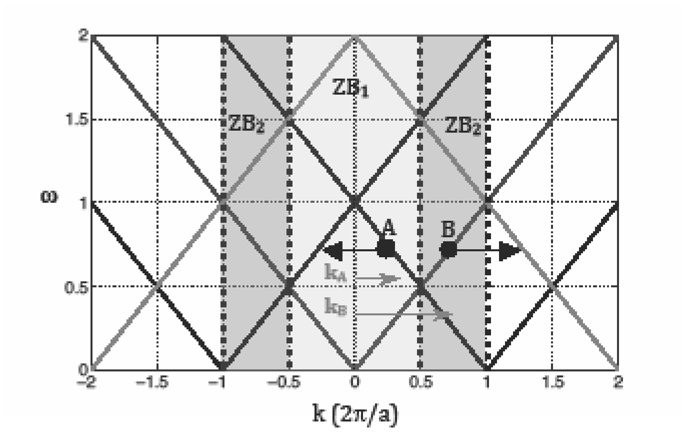


**Figure 1.13.** *Band diagram of a 1D periodic homogeneous medium presenting a positive refraction index. The bold lines represent the unfolded dispersion relation. The bold arrows are the group velocities at points A and B*

Let us now apply this principle to the case of negative refraction for the second band. As discussed recently, left-handed waves such as at point A may be identified; see Figure 1.14. However, in the unfolded diagram, we have to look at point B in the second Brillouin zone which corresponds to the same frequency and lighting condition (fixed by the construction line). In that image, the dot product of the wavevector $\mathbf{k}_B$ and the group velocity are no longer negative. For the second dispersion band, negative refraction is finally explained by the negative curvature of the EFC at point B. This conclusion enables us to generalize the concept of the curvature index that drives the beam shaping operation in PhCs.

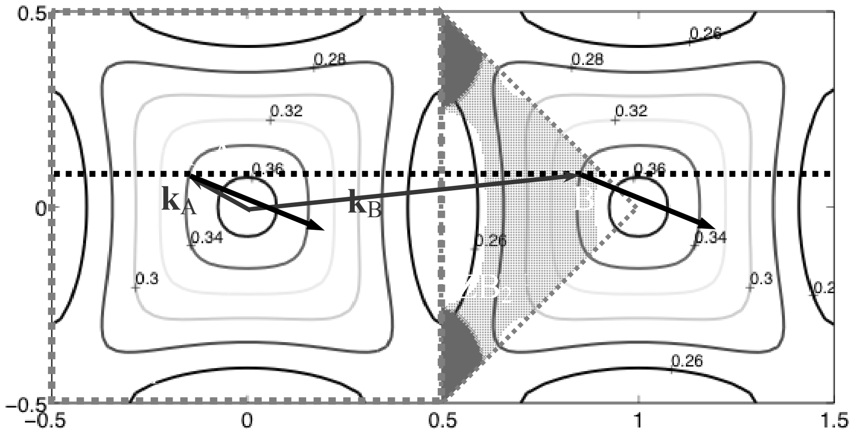


**Figure 1.14.** *EFCs of the second band. The light gray (blue in color version) and dark gray (red in color version) areas correspond to the 1st and 2nd Brillouin zones respectively. The black arrows are the group velocities at points A and B. For a color version of this figure, see www.iste.co.uk/vanbesien/nanophotonics.zip*

In conclusion, if the 1st Brillouin gives the right propagation direction followed by light in PhCs, the mechanism is quite different than for metamaterials. In the former structures, the shape of the EFCs dictates the light path and the local curvature is the pertinent optical parameter allowing a clear understanding of self-collimation and negative refraction effects.

### 1.4. From concepts to reality

For optical wavelengths (infrared down to visible), the patterning scale is sub-micron and quickly falls to very fine details of about tens of nanometers. If, at these scales, bottom-up synthesis of materials can be considered (opals or semiconductor nanowires, etc.), it quickly appears that such techniques have suffered, up to now, from the lack of regularity on a large scale, compared to the "crystal" period. Obviously, this regularity is of fundamental importance to create all the dispersion effects described in the previous sections. Too many defects in the built crystal ruins the global properties extracted from the band structure. This is why, as long as the growth control remains insufficient, researchers prefer to exploit top-down techniques, extensively using nanolithography and etching processes developed for nano-electronics. A serious drawback of these approaches (also in the bottom-up case) is that 3D matter structuring remains a true challenge. However, we will see that, in most cases, a two-and-a-half-dimensional (2D½) patterning is sufficient to promote the physical effects related to “dispersion engineering”.

### 1.4.1. *2D½ prototype design*

Reality is by essence three dimensional. Most of the functionalities described in the previous sections have been discussed for 2D geometries. The main challenge is now to transfer these effects in a real 3D prototype able to mimic the 2D behavior. This absence of “thickness” in the theoretical design, which corresponds to invariance in the third direction of space, can be emulated if the existence of a single (dominant) propagation mode, characterized by an equivalent “effective” refraction index, in the transverse plane is assumed. In such a case, at first guess, the way this mode is created does not matter. The key parameter is this effective index value generated, which becomes the “material” parameter used in the 2D design to describe the dielectric matrix (later drilled) or the dielectric pillars (surrounded by air)… Unfortunately, reality is a little bit more complex and the origin of this effective index, that will profoundly impact the potential performances of the 3D prototypes fabricated, will have to be precisely considered, notably when interfacing with the real world (at macroscopic level) and when loss issues will be addressed...

### 1.4.2. *Thick substrate versus membrane approach*

In the semiconductor-based technology, two basic schemes, both using the notion of confinement by index modulation, can be found to control light propagation in a plane: the “thick substrate approach” and the “membrane approach”. These principles are illustrated in Figure 1.15. The common feature is to trap light in a high index region.

The “thick substrate approach” takes advantage of III-V semiconductor heterostructures which permit, when properly dimensioned, an efficient light confinement for wavelengths at the micron scale (the so-called telecommunications wavelengths around 1.3-1.55 µm). Figure 1.15(a) gives a generic example of such a heterostructure grown on a InP (Indium Phosphide – $n = 3.16$) substrate. The InGaAsP core, 0.5 µm thick, is the high index region ($n = 3.36$) and is covered by a thin InP superstrate (0.2 µm thick) for symmetry and mode quality purposes. Also given in Figure 1.16 are the index profile and the electric field distribution at 1.55 µm (along the growth direction). The spatial extension of the dominant guiding mode is clearly visible, mainly within the substrate. The tail of the field distribution, which exceeds one micrometer, will have to be taken into account when the 2D patterning is considered for the photonic crystal definition. On the upper side, the extension is limited by the presence of air (n = 1) and soon becomes residual. However, both tails will have to be considered to evaluate out of plane losses (leaky waves) for a given operating wavelength exploiting a 3D prototype. For the 2D photonic crystal design, an effective index of about 3.26 can be extracted for the fundamental guided mode.

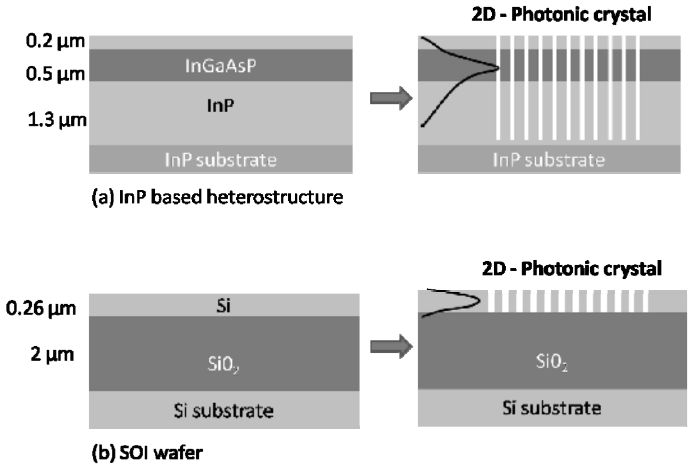


**Figure 1.15.** *Thick substrate (a) and membrane approach (b) for the realizations of 2D photonic crystals (here: air holes in a semiconductor matrix)*

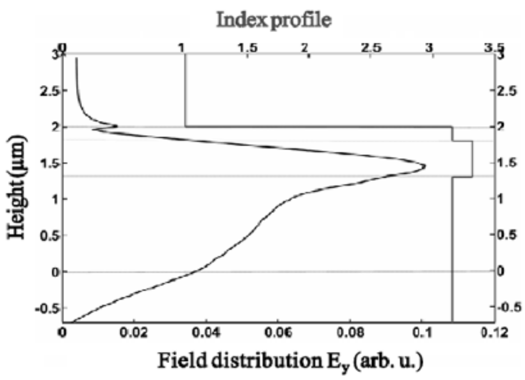


**Figure 1.16.** *Planar guides mode: index profile and field distribution in the III-V InP-based heterostructure of Figure 1.15(a)*

The “membrane approach” is more common in silicon technology. Ideally, it consists of a Si slab, properly dimensioned, surrounded by air on both sides. It is obviously the highest index contrast achievable… However, at infrared or telecommunications wavelengths, the resulting thickness of the Si slab (the “membrane”) is such that it becomes inconceivable to fabricate large enough surfaces to fulfill the size requirement of usable prototypes (a few $mm^2$ – the reasoning is also true for III-V semiconductor membranes). To circumvent the inherent fragility of such membranes, SOI (Silicon On Insulator) technology is probably the best answer. Instead of a free-standing structure, the Si slab (n = 3.45 – typically a few hundred nm) is grown on a $SiO_2$ layer (n = 1.45 – a few µm thick) deposited on a SI substrate, as illustrated in Figure 1.15(b). The high index contrast thus achieved on both sides of the Si layer drastically limits the tail of the electric field distribution and will impact the 2D crystal formation. For 2D photonic crystal design, an effective index of about 3 will be obtained for the fundamental guided mode.

### 1.4.3. *2D patterning and prototype designs*

Whatever the approach chosen, “thick substrate” or “membrane”, the definition of a 2D photonic crystal (hole or pillar arrays) at the nanometer scale to operate at infrared wavelengths results from the combination of two advanced technological tools: electronic lithography and dry etching. The main issue consists of creating, using one or several lithography steps, a hard mask representing the negative image of the patterns to be created (hole, pillar, strip, etc.) on the wafer able to resist the etching step.

Obviously, the etching step will be more critical for the “thick substrate” approach since high aspect ratios (hole or pillar diameter versus depth), higher than 10:1, will be required to capture the transverse propagating mode entirely. Conversely, small ratios, close to 1:1 or 2:1, will only be necessary for the “membrane” approach.

For the first technological step, relative to nanolithography, different strategies can be envisaged. In general, for a given application, the photonic crystal is just one of the components of the whole integrated photonic circuit. To be interfaced with the exterior world, strip waveguides of various geometries (lengths and widths) need to be added to the design. Globally, this waveguide “circuitry” represents a small surface of “material” compared to the total wafer surface. Therefore, a negative resist (for which the “written” zone remains after development) is used for the profitable use of electronic lithography. For the photonic crystal area, where filling factors are generally between 40 and 60%, the use of a positive resist can be pertinent. Also questionable is the use of an additional oxide layer ($SiO_2$ or $Si_3N_4$) as the hard mask for the etching, as is commonly done, since some negative resists, after densification by $O_2$ plasma oxidation, show very strong resistance to the etching process.

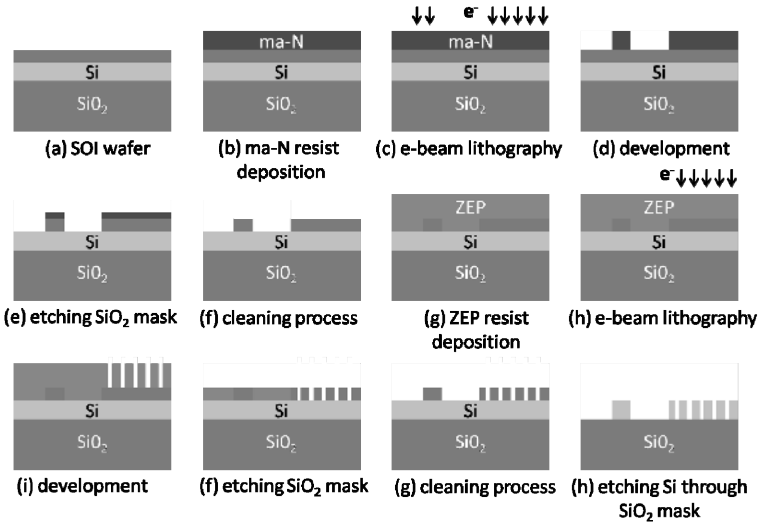


**Figure 1.17.** *Overview of the fabrication process in silicon technology of photonic crystal-based integrated devices. For a color version of this figure, see www.iste.co.uk/vanbesien/nanophotonics.zip*

To illustrate these various approaches, two typical fabrication processes of a photonic crystal along with the "strip circuitry" are detailed in the following. The first was developed at the IEF (Institut d'Electronique Fondamentale – Paris Sud University) using silicon technology, whereas the second was developed at the IEMN (Institut d'Electronique, de Microélectronique et de Nanotechnologie – University of Lille 1) using an InP-based material system.

1.4.3.1. *SOI-based process*

Figure 1.17 details the first approach developed at the IEF based on an SOI wafer. It starts with a 6 inch diameter SOI wafer, with a 260 nm Si layer and a 2 µm buried silica ($SiO_2$) layer. The wafer is then treated to obtain a 150 nm-thick $SiO_2$ layer on top of the Si layer, which will be used as a hard mask to transfer the designed pattern onto the Si layer (a). The process is divided into two main steps.

Firstly, the "strip circuitry" is defined using a 400 nm-thick negative resist (here ma-N2403) deposited by spin-coating on the SOI wafer (b). The waveguide pattern is then insolated using e-beam lithography (c). After a development phase (d), the resist pattern is transferred to the 150 nm-thick top $SiO_2$ layer using reactive ion etching (e). The sample, cleaned using $H_2SO_4$:$H_2O_2$ and $O_2$ plasma (f), is ready for the next step: photonic crystal formation.

In the second step, a 300 nm-thick positive resist (ZEP520A) is deposited by spin coating throughout the wafer (g). E-beam lithography is used to define the photonic crystal pattern (h), and after development (i), the $SiO_2$ mask is etched to define the final hard mask (j).

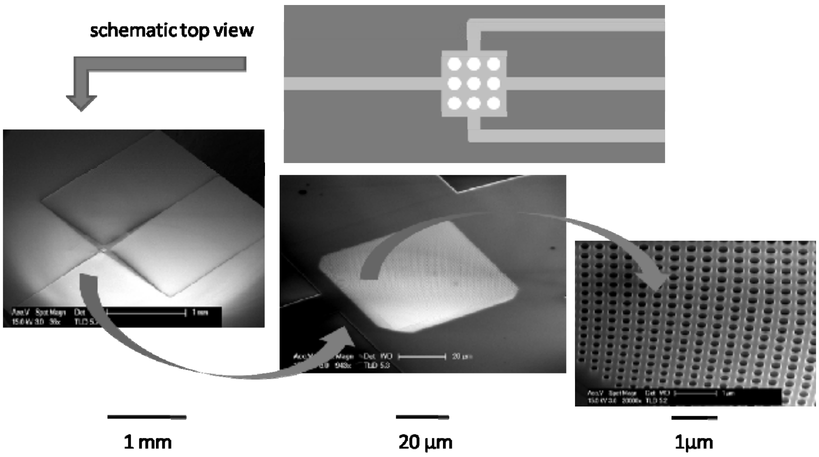


**Figure 1.18.** *Schematic top view of a photonic crystal-based device including strip circuitry in silicon technology and SEM views of fabricated samples (courtesy of IEF)*

After a second cleaning process to remove any trace of resist (k), the silicon film is finally etched through a $SF_6/O_2$ anisotropic process (l) to transfer the desired pattern in silicon. Figure 1.18 illustrates this final step giving a schematic top view of the device along with SEM images of structures fabricated at the IEF ((a) overview of the sample and (b) zoom on the photonic crystal area – let us mention that in this case, the fabrication of a graded photonic crystal with a precise control of hole dimension and distribution was targeted for wavelength multiplexing purposes; see Chapter 3.

Behind such a "simplified" presentation of the technological processes, it has to be mentioned that, due to the reduced dimensions of the constitutive elements of the device, many effects, secondary at larger scales, have to be included at the design stage to ensure properly sized prototypes at the end of the process. Among these, proximity effects (dispersion of the electron beam over a wider area than scheduled due to interaction of electrons with the resist and the substrate) require precise reverse engineering to fix both the exposure doses and the dimensions of the mask constitutive elements before achieving the theoretically targeted prototype dimensions.

Such a process can also be applied to the III-V material system. Generally, for photonic crystal definition, the hard mask is made of $Si_3N_4$ instead of $SiO_2$ and the classical positive resist used is PMMA… The major issue will here be to control the deep etching to reach high contrast ratios. We will illustrate this challenge on a simplified technological process making use of a sole negative resist as the hard mask used both for photonic crystal and strip circuitry definition.

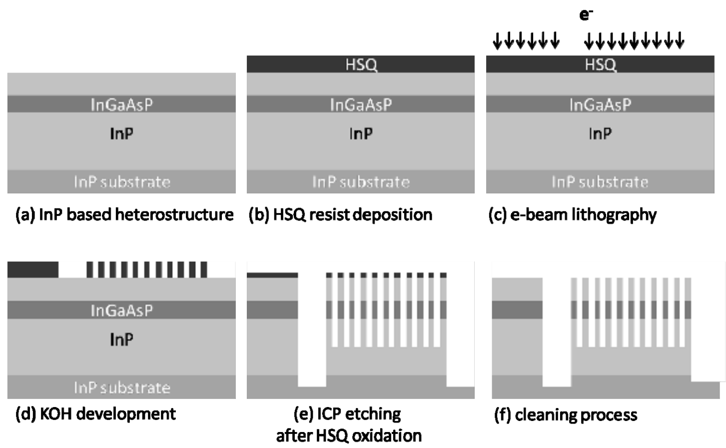


**Figure 1.19.** *Overview of the fabrication process in InP technology of photonic crystal-based integrated devices. For a color version of this figure, see www.iste.co.uk/vanbesien/nanophotonics.zip*

1.4.3.2. *InP-based process*

Figure 1.19 illustrates a simplified technological procedure using a single HSQ negative resist for lithography and etching developed for the InP-based material system developed at IEMN. From the previous process, we can observe that the area covered by the photonic crystal is small compared to the wafer surface. Moreover, the targeted filling factors (in air) are generally between 30 and 60%. In terms of e-beam exposure for the photonic crystal area, this means that the “cost” will be almost equivalent if we write the surface of future holes (positive resist) or the complementary area (negative resist). If we now turn to the whole wafer, including strip circuitry for which the use of a negative resist is mandatory, we can conclude that the use of a single negative resist to define both the crystal and the waveguides should not be detrimental in terms of electron lithography expenses… In addition, it has been shown that some negative resists, such as HSQ-FOX16 (HSQ for hydrogen silsesquioxane), can be used after densification (by oxidation) as a hard mask, showing a high etching selectivity compared to semiconductors (20 nm/min compared to 400 nm/min for InP-based material) for deep reactive ion etching. Thus, a full process can be defined without any additional oxide layer deposited on the wafer.

Starting from the epitaxial layer (a), a 500 nm-thick HSQ layer is deposited by spin coating (b). The e-beam exposure (c) is followed by a development step in KOH (d). After densification of the HSQ under $O_2$ plasma, ICP (inductively coupled plasma) deep etching using $Cl_2/H_2/CH_4$ gas is performed to transfer the desired pattern in the InP-based heterostructure (e). Let us mention that the ICP etching combines both physical and chemical etching, leading to very high etching velocities, at least 10 to 30 times higher than each process taken separately. In such a case of high aspect ratios (hole or pillar diameter versus hole or pillar depth − around 8 to 10:1), a specific issue also has to be optimized: species evacuation during etching, particularly in the photonic crystal area. As shown in (f), after the cleaning process higher etching depths are obtained in the vicinity of “big” elements such as strip waveguides than within the crystal itself. Etching is stopped as soon as the etching depth within the crystal greatly exceeds the InGaAsP quantum well position (to capture the transverse propagating mode efficiently), hoping that the depth obtained outside the crystal area is not too high with the risk of weakening the device or being detrimental for characterization purposes.

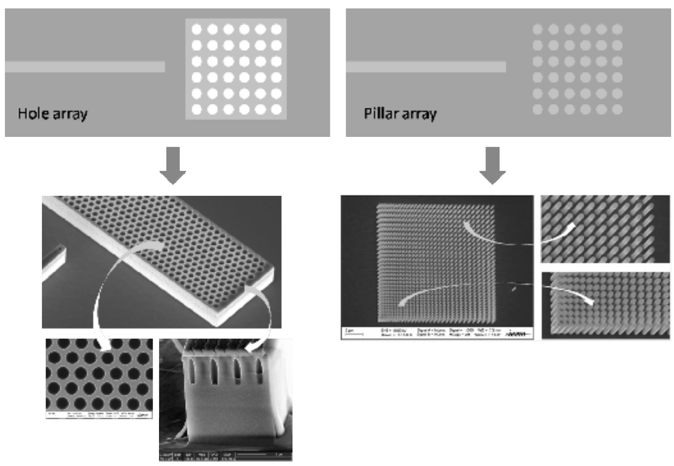


**Figure 1.20.** *Schematic top view of a photonic crystal-based device (hole and pillar arrays) including strip circuitry in InP technology and SEM views of fabricated samples (courtesy of the IEMN)*

Figure 1.20 shows samples fabricated at the IEMN using such a “one mask” process. One advantage also afforded by this process is its ability to generate hole or pillar arrays (as negative refraction base flat lenses or gradient index lenses) or mixed quasi-crystals (as 2D cloaking devices) indistinguishably, leading to a high degree of freedom in device design as will be shown in the following chapters.

### 1.4.4. *The 3D reality*

As previously mentioned, all the technological processes detailed in the previous section show the tremendous effort necessary to bring the results of the designers, essentially achieved through 2D simulations, to 3D reality. Between both approaches, the main issue concerns leaky waves and induced losses in the air above the device or within the substrate. Also of major concern is the correct interpretation of experimental data or images issued from various characterization tools, 3D in essence, which have to be transferred into the 2D world of simulations. Indeed, the 3D reality is often too complex to be correctly handled by simulation, particularly when recursive optimization procedures are required.

Concerning the loss issues, beyond the “constitutive” losses due to the materials used to fabricate the artificial structure, which can be included in 2D studies, the main difficulty is undoubtedly in correctly evaluating out of plane losses. Schematically, the key formula to undertake these effects is: $\omega = ck/n$. This gives for $n = 1$ the light line (or the light cone in a multidimensional approach) or the substrate line which can be superimposed on the dispersion diagram of the 2D crystal. If the exploited propagation mode is below these lines, confinement is perfect and losses are suppressed. In other cases, coupling with free modes is possible and propagation losses have to be qualified. In the 1990s, numerous works were devoted to the definition of lossless waveguides patterned in photonic crystals. Different strategies to push the propagating mode below the light line without degrading its velocity by adapting the guide geometry have been proposed. On the other hand, much less work can be found for devices based on dispersion engineering such as those which are the concern of this book.

Many reasons can explain this relative disinterest. Firstly, as most of the research involving dispersion engineering is in the exploratory phase, the question of performance is not of prime importance in the physicist’s mind and the theoretical and/or experimental demonstration of a “new” effect is sufficient to create a breakthrough in the field. Secondly, some effects naturally exploit modes located at or just below the light line (such as $n = -1$ negative refraction for instance). Thirdly, depending on the technology, the conclusions laid on photonic crystals, such as using deep hole etching for a thick substrate approach (III-V technology) and the SOI or membrane approach (Si technology), are assumed to remain valid. Fourthly, as one of the key factors of merit is to design miniaturized systems (even with rather complex functionalities), such propagation losses are expected to be of second order. All these reasons put together show that much remains to be done in this field to reach industrial qualification.

Nevertheless, as will be detailed in Chapter 2, the interpretation of experimental "images" often requires a profound understanding of 3D dispersion properties. This appears to be mandatory as soon as a "measurable" prototype, which includes the "active" device where physics occurs and its environment, is needed. Mixed propagation regimes (free space and/or guide), complex couplings between waves and matter, refraction/diffraction phenomena exist and render the "exploitable" information far from the "simple field map" deduced from simulation. A permanent trade-off has to be maintained between the fast 2D simulation processes required for design and optimization, and the complete 3D "exact" calculations for physical understanding, with multiple successive adjustments and much back-and-forth between both.

## 1.5. Conclusion

The aim of this first chapter was first to present, in detail, 2D dielectric photonic crystals in particular for the exploitation of the propagation properties, such as ultra-refraction or negative refraction for instance, afforded by their periodic arrangement. Secondly, the different fabrication strategies depending on the semiconductor families involved have been illustrated. The following chapters will focus on optical devices which can be imagined starting from this toolbox. Various kinds of "flat lenses" will first be investigated to open the way to more complex disposals, based on "transformation optics" techniques to go beyond pure periodic structures and reach intriguing concepts such as "invisibility". All of this will be done keeping in mind the field of integrated nanophotonics, explaining why most of designs will be developed at a 2D level even if fabrication and characterization aspects will have to be considered three-dimensionally.